Article

Asymmetrical Rotor Skewing Optimization in Switched Reluctance Machines Using Differential Evolutionary Algorithm

Jorge Torres [1,*], Pablo Moreno-Torres [2], Gustavo Navarro [1], Marcos Blanco [1], Jorge Nájera [1], Miguel Santos-Herran [1] and Marcos Lafoz [1]

[1] CIEMAT, Spanish National Research Centre on Energy, Environment and Technology, 28040 Madrid, Spain; gustavo.navarro@ciemat.es (G.N.); marcos.blanco@ciemat.es (M.B.); jorge.najera@ciemat.es (J.N.); miguel.santos@ciemat.es (M.S.-H.); marcos.lafoz@ciemat.es (M.L.)

[2] Gamesa Electric, 28830 Madrid, Spain; PABLO.MORENOTORRES@siemensgamesa.com

[*] Correspondence: jorgejesus.torres@ciemat.es

Abstract: Minimizing torque ripple in electrical machines for a given application is not a straightforward task, especially when the application imposes certain constraints. There are many techniques to improve torque ripple, either design-based or control-based. In this paper, a new geometry for switched reluctance machines based on rotor poles skewing is proposed to minimize torque ripple. This paper describes a methodology to design an asymmetrical skew rotor—switched reluctance machine using a multi-objective differential evolutionary algorithm. The main parameters of the optimization process are defined, as is the optimization methodology to obtain an improved design with less torque ripple than a conventional one. Moreover, the analytical formulas used in the optimization method, as well as the optimization technique, are deduced and explained in detail. The mathematical model used to simulate the electrical machine and the power converter are also described. Two-dimensional and three-dimensional finite element analyses were also conducted to assess whether 3D effects (end-effect and axial fringing field) affected the results. Finally, a particular case of a high-voltage direct current-controlled generator in the base of the More Electric Aircraft (MEA) concept or an energy storage system as an electrical machine was analyzed, and the results for the improved configuration were compared with those for the conventional one.

Keywords: switched reluctance machine; torque ripple; skewed rotor; differential evolution optimization; multi-objective optimization

1. Introduction

Torque ripple in electrical machines consists of variations of the instantaneous torque provided by the machine as it turns (as rotor position changes) while providing a constant average torque. Under an ideal supply (i.e., perfect current waveforms), these oscillations are periodic and are caused by factors such as cogging torque or mechanical imbalances. However, when accounting for real currents, current harmonics also contribute to generate torque ripple. The most common way to express torque ripple T_{ripple} is by the difference between the maximum and the minimum instantaneous torque during one electrical revolution (T_{MAX} and T_{MIN}) with respect to the average torque T_{AVG}; see Equation (1).

Torque ripple is generally an undesired effect in electrical machines due to its negative consequences, including mechanical vibrations, which in turn generate acoustic noise, and higher radial forces, which imply a higher load in the bearings [1–3]. All these effects can reduce the lifetime of a machine.

Switched reluctance machines (SRMs) are becoming increasingly popular as a feasible alternative to induction machines (IMs) and synchronous reluctance machines (SynRMs), especially at medium and high speeds [4]. All these machines share common advantages:

they are intrinsically sturdy and relatively insensitive to temperature due to the mechanical resiliency of their rotors thanks to the absence of windings and permanent magnets. This sturdiness is achieved by cutting torque density and energy efficiency, two of the main advantages of permanent magnet machines [5,6].

$$T_{ripple}[\%] = \frac{T_{MAX} - T_{MIN}}{T_{AVG}} \cdot 100 \tag{1}$$

where T_{ripple}: torque ripple per cent; T_{MAX}: maximum instantaneous torque during one electrical revolution; T_{MIN}: minimum instantaneous torque during one electrical revolution; and T_{AVG}: average torque.

However, there are some important differences between SRMs and IMs/SynRMs. While the former have salient poles in both the stator and rotor and use concentrated windings, the latter have cylindrical rotors and mostly use distributed windings. The shape of the rotor implies higher windage losses in SRMs [7,8], while the type of winding has consequences on the performance and robustness of the machine, arguably making SRMs the sturdiest alternative [4,5,9–15]. Additionally, SRMs can operate with just $(m - 1)$ or $(m - 2)$ phases providing $(m - 1)/m$ or $(m - 2)/m$ of power, respectively; maintaining the current reference; or even operating with a short circuit in one phase, which is not possible in IMs [16–19].

Concentrated windings make SRMs more robust, but they are also partially responsible for their main disadvantage: high torque ripple. Torque ripple in SRMs is unusually high when compared to other machine types [6]. Consequently, researchers and engineers working on SRMs have focused on torque ripple reduction for decades, obtaining many technical solutions to improve torque ripple in these machines.
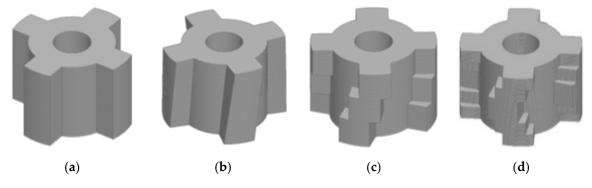
There are two main approaches to reduce torque ripple in SRMs (which can be complementary): machine design and machine control. Design solutions, such as rotor skewing and machine oversizing, imply performance loss (torque density will always be lower) [20–27]. Control solutions such as current profiling (CP, also known as current shaping) [28–32] and torque sharing functions (TSF) focus on adapting the shape of the real current pulses so that torque dips/peaks are minimized [33–40]. Other proposals use special power electronics topologies with a second DC source to increase available voltage under certain operating conditions, thus allowing for higher di/dt [33].

This work exclusively focuses on rotor skewing, which belongs to the design approach. It is the authors' opinion that control approaches should generally be favored in SRMs, as they manage to reduce torque ripple without jeopardizing machine performance. However, in those cases in which further measures are required or control approaches are not eligible, this paper proposes an asymmetrical skew method that can be optimized to improve performance compared to conventional skewing.

The skew technique is a method widely used in electric machines, especially in induction motors and permanent magnet machines. In the case of SRMs, this technique has been used and proved in many research studies [41–46], as well as in patents [47–55]. It produces benefits in the performance of the SRM, especially in relation to torque ripple, unwanted vibration (reducing the loads on the bearings), and acoustic noise. The skewed structure allows for the minimization of the radial forces suffered by the stator, thus reducing the vibrations on the structure and, indirectly, the acoustic noise developed by the machine [3,41]. Moreover, a skewed structure causes a modification of the air gap (non-uniform air gap) since the magnetic circuit in each position of the rotor is different from the conventional configuration without skew. That provokes a reduction of the tangential forces and, indirectly, a reduction of the torque ripple and average torque (shown in the paper), thereby improving the performance of the machine in relation to the vibrations and acoustic noise [3,41]. Most of the existing methods to improve the performance of SRMs were classified according to their typologies and effects on SRM performance [3].

There are different ways to skew the rotor of an electrical machine, as depicted in Figure 1. Continuously skewed rotors such as that in Figure 1b are very common in induc-

tion machines. On the other hand, step-skewed rotors (discretely skewed rotors) are the preferred solution in permanent magnet machines because they allow for shorter straight magnets instead of longer skewed magnets. Step-skewed rotors are usually symmetrical or V-shaped, such as those in Figure 1c,d, respectively. From the electromagnetic point of view, both the symmetrical and V-shaped configurations are practically equivalent in most cases, since any lamination configuration can be rearranged to obtain the other. Moreover, the steps of the laminations are fixed and equal, i.e., each package of amination has the same length. However, their mechanical and aerodynamic behavior is rather different.

| (a) | (b) | (c) | (d) |

Figure 1. Different types of 4-pole SRM rotors: (**a**) non-skewed rotor, (**b**) continuously skewed rotor, (**c**) symmetrical step-skewed rotor, and (**d**) V-shaped step-skewed rotor.

All these skewing methods are not suitable for SRMs, as they are not optimized to reduce torque ripple while minimizing the loss of average torque (and thus of torque density and power density). In this work, an asymmetrical step-skewed rotor for SRMs (ASR-SRM; see Figure 2) is proposed in an attempt to improve this aspect, along with a methodology to optimize this configuration. The differences with respect to conventional skewing methods are the dissimilar lengths of the packages and skew angles. This new configuration is explained in Section 2.1.
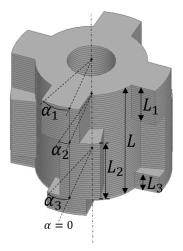

Figure 2. Proposed asymmetrical step-skewed rotor of an SRM (ASR-SRM): layout and main parameters.

The topology used in this paper was a 6/4 SRM, the most common one used in research papers and industrial products. However, the proposed methodology could be applied to other SRM topologies such as 8/6, 4/2, and 10/8.

The paper presents a design methodology for an asymmetrical skew rotor-switched reluctance machine (ASR-SRM) using a multi-objective differential evolutionary (DE) algorithm in order to reduce torque ripple. This methodology, which includes the calculation of the phase activation or switching angles, was applied to a study case that compared the results with a conventional SRM rotor design. The study case was related to two of

the applications more studied for an SRM in last decade: the first, the use of an SRM in an energy storage system as electrical machine and, the second, the use of an SRM generator as high-voltage direct current-controlled generator (HVGEN) applied to the More Electric Aircraft (MEA) concept. Both applications require a high-speed machine with high-performance configuration and robustness, as well as the possibility to work in harsh environments (high temperature, low pressure, overload, etc.). This paper describes the methodology of the ASR-SRM process design for an R&D prototype, thus the maximum performance of the machine is a goal and their cost is in a second place.

The rest of the paper is organized as follows: In Section 2, the hypotheses and simplifying assumptions are presented and assessed by finite element method (FEM) simulations. The model implemented for the study is described in Section 3. The optimization methodology and a particular case are proposed in Section 4. Moreover, the simulation results are presented and compared with the conventional configuration. A study case comparing the results of both configurations is described in Section 5. Finally, some conclusions are provided in Section 6.

2. Asymmetrical Skew in Switched Reluctance Machines

2.1. Description

The proposed skewing method consists of using N packages of magnetic laminations of lengths $l_1, l_2, \ldots l_n$ and skewing angles $\alpha_1, \alpha_2, \ldots \alpha_n$, as shown in Figure 2. These angles are defined with respect to the original position of a non-skewed rotor, $\alpha = 0°$, which is the angle reference for the control system and therefore the one used to activate machines phases [34,56]. This skewing method is actually a generalization of the conventional step-skewed approach, in which all the lengths are the same ($l_1 = l_2 = \ldots = l_n$) and in which the absolute value of the difference between two consecutive angles is constant ($|\alpha_1 - \alpha_2| = \ldots = |\alpha_{n-1} - \alpha_n|$). This implies that the skew angle step is fixed for a specific rotor configuration.
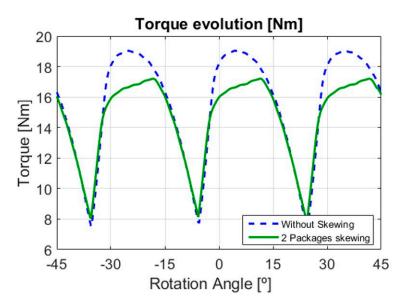
Using variable lengths ($l_1, l_2, \ldots, l_n$) and variable angles ($\alpha_1, \alpha_2, \ldots, \alpha_{n-1}, \alpha_n$) allows for the further optimization of rotor geometry, which is why the proposed skewing method might provide better performance than classical alternatives. The comparison results for both skewing methods are presented in Section 3.

The typical control strategy for an SRM is an advanced hysteresis-band based strategy, explained in Section 3. This control improves the performance of the machine (higher average torque and ripple reduction by means of phases overlapping). In this work, current profiling (CP) and torque sharing functions (TSF) were not considered. This study focused on the effects of skewing on torque ripple without interactions with the CP and TSF techniques. Additionally, these techniques are difficult to apply to high-speed high-power applications [36,38].

2.2. Lengths and Angles Optimization: 2D Approach

This section presents an optimization procedure for maximizing the average torque while reducing the torque ripple. The proposed solution would lack practical interest if the optimization process was burdensome and complicated. Therefore, a simplified approach was adopted in the paper: end-effects and 3D-effects were neglected. This means that the torque-angle characteristic of the SRM could be decomposed into N different curves or components corresponding to the N packages of rotor laminations. This hypothesis is tested in Section 2. Under this assumption, the length of each package (l_i) defines the amplitude of the corresponding torque component ($T_i(\theta)$), while the phase difference between the original torque-angle characteristic ($T_{ref}(\theta)$) and each torque component curve ($T_i(\theta)$) is given by the skewing angle (α_i).

The reference torque curve (T_{ref}) was obtained from a multi-static FEM simulation analysis (base case configuration) in which the current reference was fixed ($I_N = 260$ A) and the angular position was changed, thus completing an electrical revolution, to calculate

the torque value at each position. The result was the torque curve shown in blue in Figure 3 (base case).

Figure 3. 2D torque curve without skewing (dashed blue line); 2D torque curve with 2 skewing packages (green line). In the paper, continuous lines represent analytical results, while dashed lines represent FEM results.

The case of decomposition in two packages (see Figure 3) was based on Equations (2)–(8). The boundary constraints of the optimization process for two packages (the optimization process and methodology for N packages is described in detail in Section 3) are defined in Equation (8). The range of skewing angles is a designer selection that should be defined based on analysis experience. Notice that increasing skewing angles beyond a certain point makes little sense, since skewing angles provide diminishing returns with respect to torque ripple while the average torque reduction becomes more pronounced. Based on experience with previous optimizations, it is convenient to define a limited range to avoid exploring a large area of solutions during the optimization process. The maximum and minimum physical skewing angles for an SRM are calculated using Equation (9). In this case, the range for skewing angles was set within $[-20°, 20°]$.

$$l_1 + l_2 = l \tag{2}$$

$$\frac{l_1}{l} + \frac{l_2}{l} = s_1 + s_2 = 1 \tag{3}$$

$$T_1(\theta) = T_{ref}(\theta + \alpha_1) \cdot s_1 \tag{4}$$

$$T_2(\theta) = T_{ref}(\theta + \alpha_2) \cdot s_2 \tag{5}$$

$$T_j(\theta) = T_1(\theta) + T_2(\theta) \tag{6}$$

$$T(\theta) = \sum_{j=1}^{m} T_j(\theta) \tag{7}$$

$$\alpha_1, \alpha_2 \in [-20°, 20°] \tag{8}$$

$$\alpha_{max} = \pm \frac{360°}{2 \cdot N_r} \tag{9}$$

where l_1: length of the first skewing package; l_2: length of the second skewing package; s_1: length coefficient (length per unit with respect to the total rotor length) of the first skewing package; s_2: length coefficient (length per unit with respect to the total rotor length) of the second skewing package; $T_1(\theta)$: torque component of the first skewing package; $T_2(\theta)$:

torque component of the second skewing package; T_{ref}: torque amplitude for an SRM without skewing, i.e., torque curve for a phase of an SRM without skewing (blue curve of Figure 3); $T_j(\theta)$: total torque amplitude of a machine phase; $T(\theta)$: total torque of an SRM; m: number of phases in the SRM device; α_1: skewing angle for the first skewing package; α_2: skewing angle for the second skewing package; α_{max}: maximum physical angle for an SRM; and N_r: number of rotor poles.

2.3. Asymmetrical Skew Hypothesis Validation with FEM Simulations

This section focuses on the validation of the three considered hypotheses: three-dimensional (3D) effects are negligible, the superposition principle is applicable, and the torque/flux tables of a skewed package are lagged with respect to those of an un-skewed package by an angle equal to the skewing angle. All of them are presented and validated in the next paragraphs.

Relevant aspect of FEM simulations are 3D effects (end-effect and axial fringing field) and how considering them increases model complexity, computation time, and memory and CPU requirements [57–60]; see Appendix A. It is therefore very convenient to neglect 3D effects. Generally, an SRM design should be performed using 3D simulations, unless the predominant effects of a 3D simulation are negligible [60]. This occurs in most standard machines when the ratio between the active length and the radius of the rotor is larger than 1. In cases where most packages are less than 5% of the axial length, the 3D effects could be relevant since their lengths are smaller than the total length.
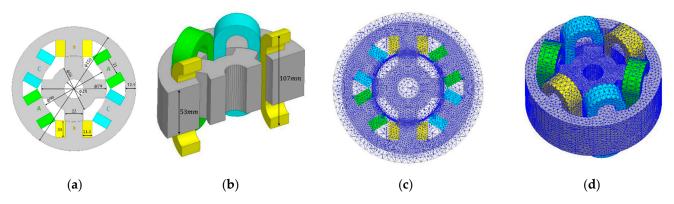
In order to verify this first hypothesis, 2D and 3D simulations were carried out using an FEM program (ANSYS Maxwell [61]). Both simulations had the same characteristics: design parameters, boundary conditions, and equivalent mesh sizes. In this sense, in both cases, the mesh refinement was performed until the results were mesh-invariant; see Appendix A. The machine parameters are collected in Table 1 and shown in Figure 4a,b. The materials used to make the machine were selected by considering the application requirements (maximum performance, high speed, and low losses). Therefore, Litz wire and high performance electrical steel (NO10) were set in order to have low losses at high frequencies. The FEM models are shown in Figure 4c,d.

Types of materials other than coil wire and electrical steel could be used since the designed process is not limited to a specific material. Conventional materials such as aluminum wire, copper bars, and copper wire for coil wire or M270-35A, M250-50A, and M400-50A for electrical steel could be used in order to reduce manufacturing costs.

The simulation results were the torque-angle characteristics, which were sufficiently similar. Table 2 collects the results for the average torque, torque ripple, and relative error between both simulations.

Table 1. SRM design parameters.

Type	Switched Reluctance Machine (SRM)
Topology	6/4
Number of phases (m)	3 (A,B,C)
Phase current (I_N)	260 A
Rated power (P_N)	20 kW
Operational speed range	[0–12,000] rpm
DC-link voltage (V_{DC})	270 V
Outer rotor diameter	79 mm
Air gap	0.5 mm
Outer stator diameter	150 mm
Active length (l)	53 mm
Number of coil turns	12
Rotor and stator material	NO10
Steel laminations thickness	0.1 mm
Coil wire	Litz wire

Figure 4. (**a**,**b**) 2D and 3D SRM design schemes with the geometrical parameters and basic layout of the FEM model: (**c**) 2D mesh model and (**d**) 3D mesh model.

Table 2. Mean torque, torque ripple, and relative errors between 2D and 3D simulations.

Skewing	Type	Mean Torque (Nm)	Torque Ripple (%)
No	2D simulation	15.56	74.70
	3D simulation	14.59	78.17
-	Relative error (%)	+6.65%	−4.43%

The results suggested that, for the particular machine used in this work, 2D simulations could be used in the rotor skew design and the optimization process instead of cumbersome 3D simulations.

Regarding the superposition theorem, the objective was to apply it to an ASR-SRM. This effect was carried out by multiplying each curve by the length factor (s_i) and then adding the torque components for all packages (see Equations (4) and (5)). The application of the superposition principle implied neglecting 3D effects between the different rotor step packages and the effects described before. Notice that the higher number of skewing packages, the more important 3D effects between packages and, consequently, the bigger error. The third hypothesis was related to the possibility of applying an angular offset to the torque and flux curves. This process is widely used in SRMs [62,63] to model and calculate the magnetic and mechanical characteristics of each phase of the machines without the need to analyze all the machine phases.

Both hypotheses had to be verified using the results obtained in the 2D and 3D simulations for the SRM in Figure 4. These results were compared with those obtained from the simulation of a three ASR-SRM design packages, the parameters of which are listed in Table 3 (skew angles are defined with respect to the original position shown in Figure 2).

$$\sum_{i=1}^{N} \frac{l_i}{l} = \sum_{i=1}^{N} s_i = 1 \tag{10}$$

$$T_i(\theta) = T_{ref}(\theta + \alpha_i) \cdot s_i \ \forall i = 1 \ldots N \tag{11}$$

$$T_j(\theta) = \sum_{i=1}^{N} T_i(\theta) \tag{12}$$

$$T(\theta) = \sum_{j=1}^{m} T_j(\theta) \tag{13}$$

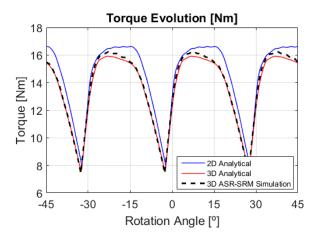$$T_{AVG} = \overline{T(\theta)} = \frac{\sum_{1}^{p} T(\theta)}{p} \tag{14}$$

$$\alpha_i \ \epsilon \ [-20, 20°] \ \forall i = 1 \ldots N \tag{15}$$

where l_i: length of ith skewing package; s_i: length coefficient (length per unit with respect to the total rotor length) of the ith skewing package; $T_i(\theta)$: torque component of the ith skewing package; α_i: skewing angle for the ith skewing package; and p: number of samples of the torque vector in an electrical turn.

Table 3. Lengths and skew angles of the chosen ASR-SRM design.

s_1 (%)	10%	α_1	18°
s_2 (%)	85%	α_2	2°
s_3 (%)	5%	α_3	19°

The results of applying the second and third hypotheses (using Equations (10)–(13)) were compared with those obtained from the 3D FEM simulation of the ASR-SRM design, shown in Figure 5. In this figure, three different curves are depicted.

Figure 5. Torque-angle characteristics for the 2D analytical superposition (blue line), 3D analytical superposition (red line), and 3D ASR-SRM (dashed black line).

- The blue line is the result obtained from the application of Equations (10)–(13) in the case of three packages. The torque reference is the torque curve obtained from a 2D FEM simulation in which the machine had a conventional configuration without skewing.
- The red line is the result obtained from the application of Equations (10)–(13) in the case of three packages. In this case, the torque reference is the torque curve obtained from a 3D FEM simulation in which the machine had a conventional configuration without skewing.
- The dashed black line is the result obtained from a 3D FEM simulation for an ASR-SRM.

The last step of the verification was to extract the relative error between the results obtained from the use of the hypotheses and those from the ASR-SRM FEM simulation. The results of calculating the relative error between the SR-SRM 3D simulation (dashed black line in Figure 5) and the other two (2D and 3D analytical ones) are collected as a summary in Table 4.
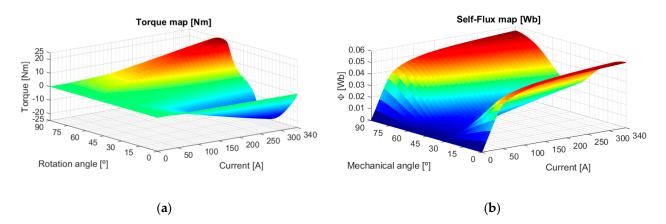
Table 4. Mean torque, torque ripple, and relative errors between for 2D and 3D superposition with respect to ASR-SRM 3D simulations.

Skewing	Calculation Method	Mean Torque (Nm)	Torque Ripple (%)
Yes	2D analytical	14.51	60.1
	3D analytical	13.61	61.7
	3D simulation	13.78	63.93
-	Relative error (%) 2D analytical	5.31%	5.98%
	Relative error (%) 3D analytical	1.19%	3.49%

In view of the results from Table 4, the following conclusion can be drawn: using a superposition-based analytical approach (Equations (10)–(13)) based on a torque curve obtained by 2D FEM simulation can be considered a valid choice for the design process, since its relative error was below 6% for this particular case of three packages. However, it should be noticed that this error would increase with the number of rotor skewing packages. For a higher number of packages, the 2D analytical approach should be replaced by the 3D analytical approach.

3. Switched Reluctance Machine Modeling

3.1. Finite Element Method Analysis for SRM

The SRM from Table 1 was modelled in Simulink. Flux and torque look-up tables (LUTs), calculated by means of 2D FEM analysis with ANSYS Maxwell [61], were used when implementing the SRM model. The layout of the SRM model is depicted in Figure 4, where letters A, B, and C represent each machine phase. The results obtained from FEM simulations—torque and flux linkage maps—are depicted in Figure 6.

(**a**)   (**b**)

Figure 6. FEM simulation results: (**a**) torque map of a machine phase as a function of current and angle; (**b**) flux map of a machine phase as a function of current and angle.

3.2. Mathematical SRM Model

A MATLAB-Simulink model was implemented to do the optimization process and analyze an SRM drive by simulation. The model included the power converter, the control strategy, and the SRM, as shown in Figure 7. This mathematical model was experimentally validated for a 25 kW, 13,000 rpm machine prototype, as shown in Figure 8.
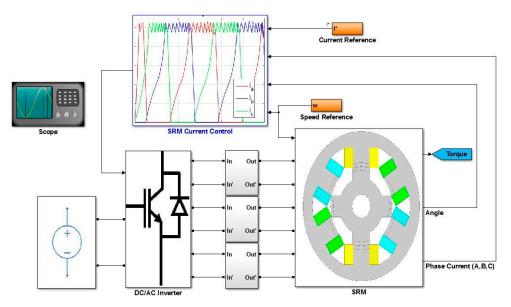
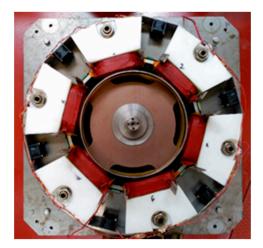**Figure 7.** MATLAB-Simulink SRM model layout.

Figure 8. The 6/4 SRM prototype used to validate the mathematical model.

The model was divided into three main parts:

1. Power electronics: the power converter model [56,64,65] had to satisfy two main objectives. The first was to implement a proper interface converter (the selection of the proper commercial IGBT branch and cooling turbine for the voltage and current levels; see Table 1), and the second was to calculate the power converter losses (including switching losses and conduction losses in the IGBTs and diodes) [34,66]. Commercial semiconductors (SEMiX305GD07E4 [67]) were used. The topology of the converter is shown in Figure 9. A converter with three half-bridge IGBTs, with one connected to each SRM phase, was considered [34]. Though other alternative topologies exist (such as the Miller topology [56]), those are focused on reducing the number of semiconductors at the expense of losing control flexibility and phase independence. It is preferred to keep full controllability by means of the half-bridge topology.

2. Control strategy: the electrical machine was current-controlled by means of hysteresis-band strategy; see Figure 10. The current evolution in a saturated switched reluctance machine is calculated using Equation (16) [65]. The higher the speed, the lower the commutation frequency. At high and very high speeds (above 8000 rpm), the hysteresis band strategy could become a single-pulse operation mode (depending on the current reference level and the design performance of the SRM), which means that

there is only one commutation per phase activation. As a result, the commutation losses at the converter and the hysteresis losses at the machine are reduced.

$$\frac{di}{dt} = \frac{V_{dc} - R \cdot i - \omega \cdot \frac{d\phi}{d\theta}}{\frac{d\phi}{di}} \tag{16}$$

where $\frac{di}{dt}$: current variation with time; V_{dc}: DC-link voltage; R: coil resistance; i: instant current; ω: angular velocity; $\frac{d\phi}{d\theta}$: inductance variation with angular position; and $\frac{d\phi}{dt}$: inductance variation with time.

3. SRM model: Due to the high nonlinear characteristic of an SRM, it is difficult to establish a mathematical nonlinear model. In this paper, a conventional model for an SRM with skewing is proposed. Therefore, the calculation of flux linkage could be performed by linear superposition [62,63]. For example, the flux linkage of phase A was calculated using Equation (17), in which the mutual inductance between phases was considered. Based on that, the flux linkage of the SRM considering mutual inductance is given by Equation (18). The crossed terms of the matrix are equal due to symmetry (i.e., $M_{AB} = M_{AC} = M_{BC} = M_{BA} = M_{CA} = M_{BC} = M$). Usually, self-inductance is at least one order of magnitude higher than mutual inductance, which suggests that mutual terms could be neglected in the optimization process.

$$\phi_A = L_A \cdot i_A + M_{AB} \cdot i_B + M_{AC} \cdot i_C \tag{17}$$

where ϕ_A: flux linkage of phase A; L_A: self-inductance of phase A; M_{AB}: mutual inductance between phase A and phase B; M_{AC}: mutual inductance between phase A and phase C; i_A: phase current of phase A; i_B: phase current of phase B; and i_C: phase current of phase C.

$$\begin{bmatrix} \phi_A \\ \phi_B \\ \phi_C \end{bmatrix} = \begin{bmatrix} L_A & M & M \\ M & L_B & M \\ M & M & L_C \end{bmatrix} \cdot \begin{bmatrix} i_A \\ i_B \\ i_C \end{bmatrix} \rightarrow \overline{\varnothing} = \overline{\overline{L}} \cdot \overline{i} \tag{18}$$

where ϕ_B: flux linkage of phase B; ϕ_C: flux linkage of phase C; L_B: self-inductance of phase B; L_C: self-inductance of phase C; and M: mutual inductance between two phases.
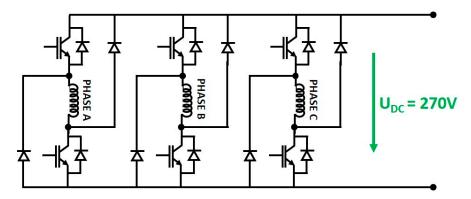

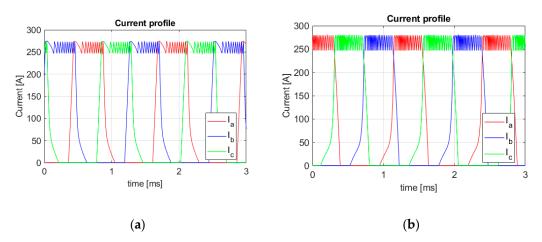**Figure 9.** 3 H-bridge machine-side power converter.

(**a**)　　　　　　　　　　　　　　　　　　　　　　(**b**)

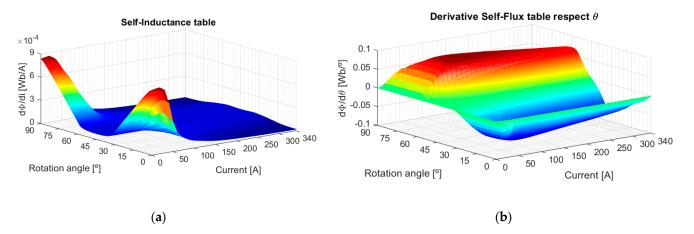**Figure 10.** Phase currents in the SRM in (**a**) motor mode and (**b**) generator mode.

Based on Equation (18), flux linkages for an SRM with skewing on the rotor (ASR-SRM configuration) could be calculated with Equation (19). This expression is based on Equations (10)–(15), and the considered assumptions are those listed in Section 2.

$$\overline{\phi} = \sum_{j=1}^{N} \frac{l_j}{l} \cdot \left[\overline{\overline{L(\theta - \alpha_j)} \cdot \overline{i}} \right] = \sum_{j=1}^{N} s_j \cdot \left[\overline{\overline{L(\theta - \alpha_j)} \cdot \overline{i}} \right] \tag{19}$$

where $\overline{\phi}$: flux linkage vector; l_j: length of *j*th skewing package; s_j: length coefficient (length per unit with respect to the total rotor length) of the *j*th skewing package; $\overline{\overline{L(\theta - \alpha_j)}}$: inductance matrix for each skew package, delayed by their skew angle; α_j: skewing angle for the *j*th package; $\overline{i}$: phase current vector; and *N*: number of skewing packages.

Finally, the current evolution for a phase (A, B, and C) in a saturated SRM as a function of the commutation frequency (e.g., angular velocity) with a hysteresis-band strategy is shown in Equation (20). From Equations (19) and (20), the expression of the current evolution for a phase in a saturated ASR-SRM can be calculated as in Equation (21).

Therefore, there are two extra LUTs that have to be calculated before implementing the MATLAB-Simulink model. These LUTs are represented in Figure 11, in which Figure 11a shows the derivative of the self-flux linkage with respect to the phase current (self-inductance) and Figure 11b represents the derivative of the magnetic flux with respect to the mechanical angle.

(**a**)　　　　　　　　　　　　　　　　　　　　　　(**b**)

Figure 11. (**a**) Self-inductance table (i.e., self-flux derivative map with respect to phase current as a function of the current and mechanical angle); (**b**) self-inductance derivative map with respect to mechanical angle as a function of the current and mechanical angle.

A screenshot of the ASR-SRM model implemented in MATLAB-Simulink is shown in Figure 12. This model considered the switching angles, the tables depicted in Figure 11, the resistance of each coil, and the torque table in function of the mechanical angle. From this model, the current evolution and the parameters for each phase (torque, current, inductance . . .) were determined as a function of the switching angles, the skewing parameters, and the speed.

$$\frac{\partial i_A}{\partial t} = \frac{V_A - R_A \cdot i_A - \frac{\partial \phi_A}{\partial \theta} \cdot \omega - \frac{\partial \phi_A}{\partial i_B} \cdot \frac{\partial i_B}{\partial t} - \frac{\partial \phi_A}{\partial i_C} \cdot \frac{\partial i_C}{\partial t}}{\frac{\partial \phi_A}{\partial i_A}} \tag{20}$$

$$\frac{\partial i_A}{\partial t} = \frac{V_A - R_A \cdot i_A - \frac{\partial \phi_A}{\partial \theta} \cdot \omega - \sum_{j=1}^{N} s_j \cdot M(\theta - \alpha_j) \cdot \left(\frac{\partial i_B}{\partial t} + \frac{\partial i_C}{\partial t}\right)}{\sum_{j=1}^{N} s_j \cdot L_A(\theta - \alpha_j)} \tag{21}$$

where V_i: DC-link voltage on phase "i"; R_i: resistance of phase "i"; i_i: current on phase "i"; $\frac{\partial \phi_A}{\partial \theta}$: derivative of the self-magnetic flux of phase A with respect to the rotation angle; and ω: angular velocity.
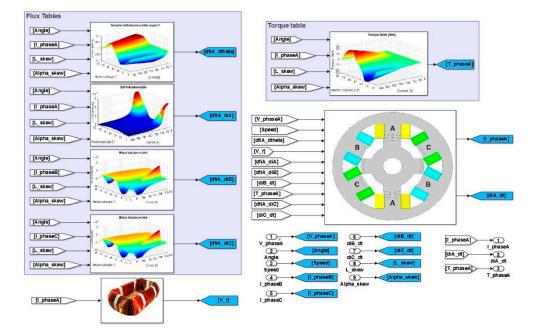

Figure 12. MATLAB-Simulink ASR-SRM model.

The torque calculation of each phase for the ASR-SRM configuration was carried out as described in Section 2, given by Equation (22). Additionally, the process used for the flux calculation was implemented as an application of the superposition principle with a mechanical angle translation. Moreover, the total torque of the ASR-SRM was the sum of the torque generated for each phase, as described by Equation (23).

$$T_i(\theta) = \sum_{j=1}^{N} T_{ref}(\theta + \alpha_j) \cdot s_j \ \forall j = 1 \ldots N , \forall i = A, B, C \tag{22}$$

$$T(\theta) = \sum T_i(\theta) \ \forall i = A, B, C \tag{23}$$

where $T_i(\theta)$: total torque amplitude of a machine phase; T_{ref}: torque amplitude for an SRM without skewing, i.e., torque curve for a phase of an SRM without skewing; and $T(\theta)$: total torque of an SRM.

4. Optimization Methodology

4.1. Description

This study presents the faces a multi-objective optimization problem that is defined as follows.

- Two objective functions: (1) torque ripple T_{ripple} (2) and mean torque T_{AVG}. The overall objective was to minimize torque ripple (calculated as described in Equation (1)) while maximizing average torque (i.e., minimizing torque loss).
- The search space of the optimization problem was composed of the length of the skewing packages (l_i) and the skewing angles (α_i). Therefore, the search space had ($2N - 1$) dimensions, where N is the number of skewing packages.
- This search space was constrained by defining the boundary conditions that determine whether a combination of skewing angles and lengths satisfies them. The results of applying these restrictions (Equation (10) for the length of the skewing package and Equation (15) for the skewing angles) are the operation ranges defined in Table 5.
- The number of skewing packages was fixed to 3 for the design proposed in this paper, since the results obtained for 2 packages were the worst and a higher number of packages (e.g., 4 or 5) would have introduced too many degrees of freedom, complicating the optimization process while obtaining similar results.

Table 5. Variables to optimize and their operation range.

s_1 (per unit)	$[0,\ 0.5]$	α_1	$[-20°,\ 20°]$
s_2 (per unit)	$[0,\ 0.5]$	α_2	$[-20°,\ 20°]$
s_3 (per unit)	$1 - l_1 - l_2$	α_3	$[-20°,\ 20°]$
α_{ON}	$[-30°,\ 30°]$	I_s	260 A
α_{OFF}	$[0°,\ 60°]$	ω	12,000 rpm

where α_{ON}: turn on angle; α_{OFF}: turn off angle; and I_s: reference current in each phase.

An advanced optimization method using a complex SRM MATLAB-Simulink model was implemented. The model includes the following, previously described characteristics.

- An SRM model with full inductance matrix, meaning that mutual effects were accounted for. Skewing effects were implemented in the calculation of the phase inductance by using the skewing angle and the length of each package.
- The model included the power electronics converter and the control strategy.
- The simulation allowed us to perform current and speed sweeps using the optimal switching angles for each operation point.
- The optimal phase activation angles for each operation point were set as the pair of values for which the machine achieved the highest torque with the least ripple. The phase activation angle reference was defined with respect to the original position of the non-skewed rotor and in an aligned position for rotor and stator poles (see Figures 2 and 4a).

The chosen optimization method was a 'multi-objective DE algorithm' [68–70] due to its simplicity, robustness, and convergence speed. This optimization algorithm, like other stochastic optimization algorithms such as genetic or particle swarm algorithms [71], works with populations (sets of solutions). These sets of solutions are iteratively modified in order to get the minimization of a user-defined objective functions. The iterative process finishes when some solutions of the population reach a certain minimum value of the objective functions or when a user-defined number of iteration is executed.

The results of the multi-objective algorithm are represented in Pareto fronts, evaluating the sets of solutions with respect to the objective functions (the average torque T_{AVG} and torque ripple, T_{ripple}). In this type of optimization, a unique optimal solution is not obtained; instead, a set of optimal solutions is found (those that form the optimal Pareto front). These solutions are considered "optimal," and the designer is in charge of determining the solution chosen within the optimal Pareto front, with some external criterion or weighting function.

The DE algorithm [68] carries out the same steps in each iteration:

1. The iteration number t starts when a trial population of solutions (Q_t) is created from the initial population (P_t); see Appendix A. The Q_t population is created following the DE crossover-mutation equations [68].
2. The new population Q_t is evaluated by calculating the objective functions values and evaluating the restrictions (if any).
3. The solutions of the population P_t and Q_t are sorted using two principal mechanisms: mutation and crossover [71]. These two mechanisms allow one to find the Pareto-optimal solutions among the $P_t + Q_t$ population.
4. The population P_{t+1} is used in the iteration $t + 1$ of the optimization process. The process continues until a fixed number of iterations is reached; see Appendix A.

Once the optimization method was fixed, the mathematical optimization problem had to be defined. The variables selected to optimize, as well as their operation ranges had to be set; both are collected in Table 5. In this study, the machine was optimized for generator mode since a high performance SRM generator is defined for the application HVGEN. Moreover, a second application of this machine is as an electrical machine of an energy storage system.

The variables of the Table 5 are the search space constrains of the optimization process. The constrains for the objective functions (maximum torque ripple T_{ripple} and minimum mean torque T_{AVG}) are described and set for this study case in Section 4. Moreover, an objective function that considers weights could be applied in order to automate and select the best configuration of the skewed rotor for the study case. An example of this function is given by Equation (24).

$$f = min\left[\left(w_1 \cdot \frac{T_{ripple}}{100} - w_2\right)T_{AVG}\right] \tag{24}$$

where f: objective function to be minimized; T_{ripple}: torque ripple of a skew configuration; w_1: weight multiplying coefficient of the torque ripple; and w_2: weight multiplying coefficient of the mean torque.

The weight coefficients are selected by designers based on application requirements. In such applications where the torque ripple reduction is in a second place and the mean torque loss has to be reduced to its minimum value, the initial values for the weight coefficients could be ($w_1 = 1$; $w_2 = 0.3$).

Notice that the conventional step-skew configurations (same lengths and absolute value of the difference between two consecutive angles; see Figure 1) were included in the possible ASR-SRM solutions (different lengths and skewing angles). Moreover, the skewed rotor study in this paper was composed of three packages, where just two were skewed since one of them was considered as the reference and only supposed a change in the switching angles, i.e., the effect of one of these packages on the skewed solution was a constant delay/advanced value of the switching angles. In summary, for the certain design of an SRM with an asymmetrical skewed rotor composed of three packages, just three lengths, two skew angles to define the rotor design, and a set of phase activation/deactivation angles could be considered. Therefore, to facilitate the comparison, a reference change of the skew angle of one of the packages was made—$\alpha_1 = 0°$ in this case, coinciding with the reference of the base case.

4.2. Evaluation Criteria

The criteria for selecting the optimal ASR-SRM configuration depends on several factors, such as the SRM characteristics, manufacturing technologies, and the chosen application, which is the most restrictive and important factor because the application sets the minimum mean torque, maximum torque ripple, and minimum power generated for the operation conditions (torque/current and rotational speed). Therefore, in this paper, the operation point was set in a current of 260 A and a speed of 12,000 rpm due to the

application requirements. The SRM was designed for this rated point since its operation cycle was near rated values, as described before. This point was the most restrictive, since both parameters achieved the highest values for the operation range of the machine (torque and speed). Moreover, the maximum torque ripple and the minimum torque (for this operation point) were fixed to 30% and 16 nm, respectively, in this study. From this restriction, the feasible area was defined as depicted in Figure 12. Once the inputs of the model and constraints were set, the Pareto front was obtained from the optimization process; it is depicted in Figure 13. The red line is the optimal Pareto front, while the black circle mark is the conventional non-skewed configuration (base case).
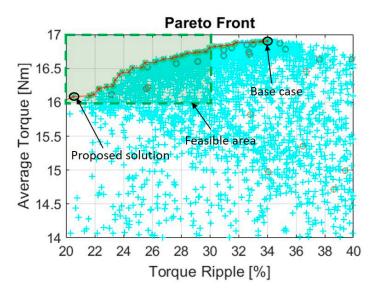

Figure 13. Pareto front, feasible area, and proposed solution for a current value of 260 A.

In applications, such as flywheels or electric vehicles (EV), in which the SRM works in cycles with a wide speed and current range, the criteria must used to achieve better performance in most of the operation points, i.e., carrying the same optimization process out but introducing speed as a new variable. This implies that the optimization process is more complex and requires more computational time since a new Pareto Front must be calculated for each operation point. Finally, a weight function has to be applied in order to select the best skewing angles for the whole operational cycle. An example of this function is given by Equation (25).

$$\overline{T}_{ripple} = \sum_{i=1}^{N_p} K_i \cdot T_{ripple}(\omega_i, I_i) \tag{25}$$

where $\overline{T}_{ripple}$ [%]: average torque ripple of a skew configuration for a defined operation range (different current and/or speed); K_i: weight multiplying coefficient; and $T_{ripple}(\omega_i, I_i)$ [%]: torque ripple of a skew configuration for a specific operation point (current and speed).

Finally, a flowchart of the process, which sums up all the steps required in the proposed methodology, is shown in Figure 14.
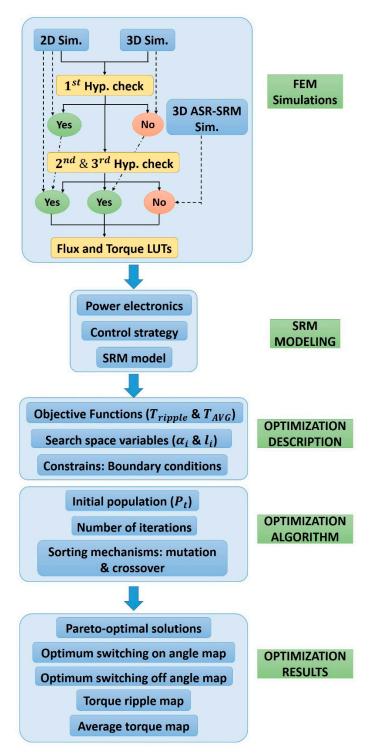
Figure 14. Flowchart of the multi-objective optimization methodology.

5. Optimization Results

5.1. Conventional SRM

The conventional configuration was chosen as a reference in this study case. The characteristics for the operation point at 260 A and 12,000 rpm are listed in Table 6. Torque ripple and average torque were found to be 34.5% and 16.9 Nm, respectively. This configuration does not comply with the restrictions detailed in Section 4 since torque ripple was above the limit.
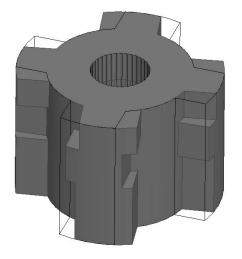
Table 6. Conventional SRM results.

Phase Current	260 A
ω	12,000 rpm
Average torque	16.9 Nm
Torque ripple	34.5%

5.2. Proposed ASR-SRM

The feasible area of possible solutions in the Pareto front shows the number of solutions that verify the application restrictions of average torque and torque ripple. The solution selected here had a significantly lower ripple than the others. The optimization variables for this solution are collected in Table 7, and a 3D design of the ASR-SRM is shown in Figure 15 (the wireframe rotor represents the conventional non-skewed design).

Table 7. Optimization variables for the chosen solution.

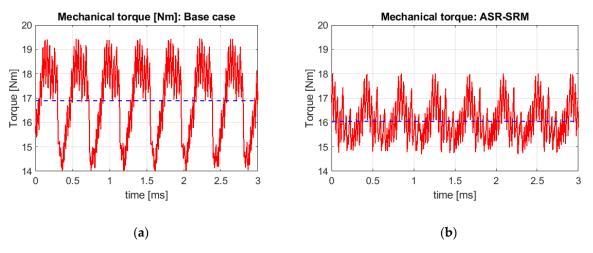|			
s_1 (per unit)	0.483	α_1	0°
s_2 (per unit)	0.29	α_2	$-6.002°$
s_3 (per unit)	0.227	α_3	2.239°
α_{ON}	$-15.479°$	ω	12,000 rpm
α_{OFF}	46.121°	I_s	260 A

Figure 15. Optimized ASR-SRM design for I = 260 A and ω = 12,000 rpm.
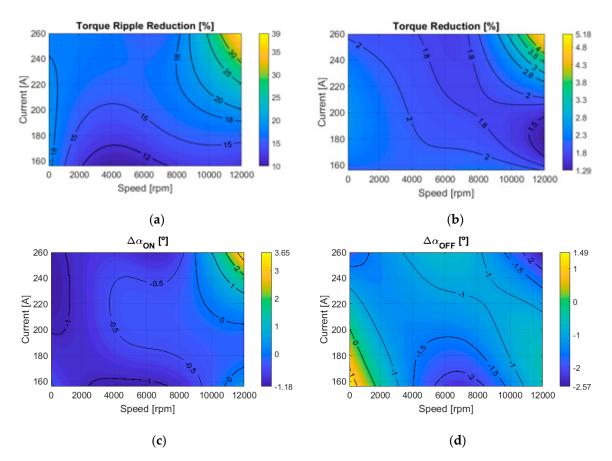
5.3. Results Comparison

Table 8 compares torque ripple and average torque for both configurations. The performance of the SRM was improved regarding the goals of the application: ripple was reduced to almost 15% in absolute terms (40% in relative terms), with a loss of less than 1 Nm in average torque (5% less torque). Figure 16 shows the torque developed by both configurations, the base case and the proposed ASR-SRM at I = 260 A and ω = 12,000 rpm. Figure 17a,b shows torque ripple and average torque reduction as a function of speed and phase current. Moreover, in Figure 17c,d, the switching on and off angle difference (i.e., the difference between the switching angle for the conventional configuration and the one used in skewing design) in both configurations (conventional and skew) is displayed.

Table 8. Optimization variables for the chosen solution.

Type	Mean Torque (Nm)	Torque Ripple (%)
Reference configuration	16.91	34.50
Proposed ASR-SRM	16.04	20.93

(**a**) (**b**)

Figure 16. Mechanical torque developed at $I = 260$ A and $\omega = 12{,}000$ rpm by: (**a**) the conventional configuration (base case); (**b**) proposed ASR-SRM configuration.

(**a**) (**b**)

(**c**) (**d**)

Figure 17. (**a**) Torque ripple reduction evolution as a function of the speed and current; (**b**) average torque reduction evolution as a function of the speed and current; (**c**) differential switching on angle evolution as a function of speed and current; (**d**) differential switching off angle evolution as a function of the speed and current.
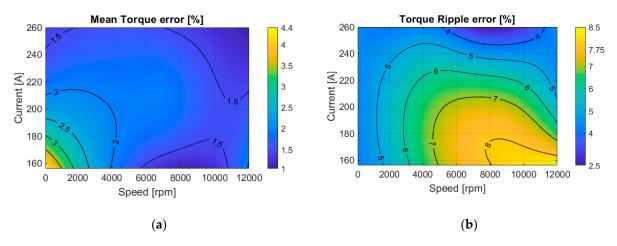
Finally, the following conclusions can be extracted from Figures 16 and 17.

- The amplitude of the mechanical harmonics was reduced and the minimum value of the torque was increased in the ASR-SRM configuration. Moreover, the proposed configuration implied a reduction on the vibrations and the loads in the bearings.
- The proposed ASR-SRM solution achieved a torque ripple reduction of more than 10% in the whole operation range (40% at rated conditions), as depicted in Figure 17a.

- This torque ripple reduction entailed an average torque reduction that was below 3% for most operating points. At rated current and speed, this reduction rose to 5%.
- The offset between the on and off angles for both configurations was practically negligible, since it was in a range of less than one degree for the entire operating range of the MRC, indicating that both configurations could operate close to the optimal performance regarding the ripple and mean torque with the same on and off angles.

5.4. D FEM ASR-SRM Results

In this section, a comparison between the results obtained from a two dimensional FEM model for the proposed ASR-SRM configuration and those obtained using a three-dimensional FEM model is made. The results of this comparison are the errors of considering the flux tables from a 2D FEM model instead of those from a 3D model. Figure 18 shows both the mean torque and torque ripple estimation errors.

(**a**)　　　　　　　　　　　　　　　　　　　(**b**)

Figure 18. (**a**) Mean torque error when considering 2D FEM simulations instead of 3D ones as a function of the speed and current; (**b**) torque ripple error when considering 2D FEM simulations instead of 3D ones against the speed and current.

From Figure 18, several conclusions could be extracted.

- The error of using a two-dimensional model to determine the mean torque of an SRM such as the one studied was within 5% of the average value in the working range of the machine. This error was due to neglecting the 3D effects in two-dimensional models. These effects could be smoothed out on large machines, i.e., the staking length could be much higher than the radial size.
- On the other hand, the maximum torque ripple was near 9%, with an average value of 6%. Both errors could be reduced by introducing the correction factors on the two-dimensional flux and torque tables used, allowing for the correction of the three-dimensional effects in this type of machine. However, as mentioned in the previous point, the error was reduced when increasing the size of the SRM.

6. Conclusions

In this paper, the authors presented a new type of rotor skewing method to reduce torque ripple in switched reluctance machines. A methodology to optimize the design of an asymmetrically-skewed switched reluctance machine is proposed. The main parameters of the proposed skewing technique (lengths and skewing angles of the rotor lamination packages), as well as the analytical equations that model this skewing configuration, were described. The skewing method consists of using a number of magnetic packages of arbitrary lengths and skewing angles so that the whole rotor design is optimized in terms of average torque and torque ripple. To define the lengths and skewing angles of these packages, an optimization process based on a multi-objective differential evolutionary algorithm was developed. This algorithm aims to minimize torque ripple while maximizing

average torque. The optimization can be achieved by considering a global model of the switched reluctance drive, including machine geometry, control strategy, and power electronics. This implies not only the use of real current waveforms but also that the machine's switching angles are optimized for each operating point and skew design (skewing angles and lengths). The paper includes a case example in which the original non-skewed design was improved towards the goals of a real application.

The results shown in Section 5 indicate that this proposed skewing method improved the performance of the conventional SRM. The torque ripple was reduced to almost 10% in absolute terms (40% in rated conditions) for the whole operation range, with an average torque reduction below 3% for most operating points (5% in rated conditions).

The asymmetrical skew rotor design was shown to directly reduce the radial forces and indirectly reduce the vibrations of the SRM. This effect was found to improve the performance of this type of machine, allowing for the use of a magnetic bearings together with an SRM in a high-speed ESS. Moreover, this configuration was shown to reduce the fatigue loads on the guiding system.

Finally, this skewing method is easy to implement in the machine manufacture process, since it does not add an important additional cost and the performance of the machine is improved. In a single- or two-phase SRM, this skewing method could improve SRM performance since it reduces the torque dead-zone.

7. Patents

The patent with the reference ES2589155A1 entitled 'Procedimiento de obtención de una máquina de reluctancia con rizado de par mejorado' [55] describes the new proposed geometry for a switched reluctance machine. The patent details the main parameters of the asymmetrical skew rotor and the differences with the conventional skew rotors implemented in electrical machines.

Appendix A

The simulation parameters for the 2D and 3D simulations are collected in Table A1. Moreover, the data for the optimization process are listed in Table A2. In each case, the current is changed from 0 A to 30% up to its maximum value ($1.3 \cdot I_s$) to model the SRM performance at high saturated scenarios.

Notice that the zones in which the mesh size has to be very low are the stator and rotor poles and the air gap near both poles since the gradient of the magnetic induction is very high, and indirectly the resultant error in those zones could be very high. An initial value for a mesh element could be the value of the air divided by 4, i.e., there are at least 4 elements in the air gap to calculate with high accuracy the magnetic induction field. In large air gaps, the number of elements could be high than 4 to represent the induction field with accuracy.

Table A1. Parameters values for 2D and 3D simulations.

Variable	2D Sim.	3D Sim.	3D Skew Sim.
Computational time	1 day	3 weeks	5 weeks
Time step (Δt)	$\frac{t_{end}}{900}$	$\frac{t_{end}}{200}$	$\frac{t_{end}}{200}$
Total simulation time (t_{end} [s])	$\frac{\frac{360°}{N_r}}{6 \cdot \omega \,[\text{rp}m]}$	$\frac{\frac{360°}{N_r}}{6 \cdot \omega \,[\text{rpm}]}$	$\frac{\frac{360°}{N_r}}{6 \cdot \omega \,[\text{rpm}]}$
Current Step (ΔI)	10 A	10 A	10 A
Angular step ($\Delta \theta$)	$\frac{\frac{360°}{N_r}}{900}$	$\frac{\frac{360°}{N_r}}{200}$	$\frac{\frac{360°}{N_r}}{200}$
Conductor type	Stranded	Stranded	Stranded
Type of simulation	Transient	Transient	Transient
Speed (ω)	Constant	Constant	Constant
Solver error	10^{-6}	10^{-6}	10^{-6}
Air gap element size	$\frac{gap}{4}$	$\frac{gap}{4}$	$\frac{gap}{4}$
Number of elements	20.000	400.000	700.000

Table A2. Parameters for optimization algorithm.

Initial population	36 samples
Number of iterations	150

In the rotor and stator poles, the problem is the same as in the air gap. Therefore, the same solution could be applied and the pole surface is meshed with a gradient in which the element size near the air gap is smaller than near the yoke.

Another point taken into account is the poles zones between different packages (in the skewed rotor simulation) where the gradient is very high and the magnetic path in the axial direction (in a particular angular position) could be different due to the variable skewing angles of the packages and also the air gap. In these cases, the element size needs to be very small to calculate the gradient of the magnetic field with the enough accuracy.

References

1. Hinterdorfer, T.; Schulz, A.; Sima, H. Force Prediction and Radial Force Compensation of a Switched Reluctance Motor. In Proceedings of the IECON 2013—39th Annual Conference of the IEEE Industrial Electronics Society, Vienna, Austria, 10–13 November 2013; pp. 2875–2880.
2. Choudhury, M.D.; Ahmed, F.; Kumar, G.; Kalita, K.; Tammi, K. Design methodology for a special single winding based bearingless switched reluctance motor. *J. Eng.* **2009**, *1*, 274–284. [CrossRef]
3. Gan, C.; Wu, J.; Sun, Q.; Kong, W.; Li, H.; Hu, Y. A review on machine topologies and control techniques for low-noise switched reluctance motors in electric vehicle applications. *IEEE Access* **2018**, *6*, 31430–31443. [CrossRef]
4. Tenconi, A.; Vaschetto, S.; Vigliani, A. Electrical machines for high-speed applications: Design considerations and tradeoffs. *IEEE Trans. Ind. Electron.* **2014**, *61*, 3022–3029. [CrossRef]
5. Jack, A.G.; Mecrow, B.C.; Haylock, J.A. A comparative study of permanent magnet and switched reluctance motors for high-performance fault-tolerant applications. *IEEE Trans. Ind. Appl.* **1996**, *32*, 889–895. [CrossRef]
6. Zeraoulia, M.; Benbouzid, M.E.H.; Diallo, D. Electric motor drive selection issues for HEV propulsion systems: A comparative study. *IEEE Trans. Veh. Technol.* **2006**, *55*, 1756–1764. [CrossRef]
7. Calverley, S.D.; Jewell, G.W.; Saunders, R.J. Aerodynamic losses in switched reluctance machines. *IEE Proc. Electr. Power Appl.* **2000**, *147*, 443. [CrossRef]
8. Romanazzi, P.; Howey, D.A. Air-Gap Convection in a Switched Reluctance Machine. In Proceedings of the 2015 Tenth International Conference on Ecological Vehicles and Renewable Energies (EVER), Monte Carlo, Monaco, 31 March–2 April 2015; pp. 1–7.
9. Mitcham, A.J.; Grum, N. An integrated LP shaft generator for the more electric aircraft. In *IEE Colloquium on All Electric Aircraft (Digest No. 1998/260)*; IET: London, UK, 1998; pp. 8/1–8/9.
10. Mitcham, A.; Cullen, J. Permanent Magnet Generator Options for the More Electric Aircraft. In Proceedings of the International Conference on Power Electronics Machines and Drives, Bath, UK, 16–18 April 2020; pp. 241–245.
11. Sebastian, T. Temperature effects on torque production and efficiency of PM motors using NdFeB magnets. *IEEE Trans. Ind. Appl.* **1995**, *31*, 353–357. [CrossRef]

12. Tariq, A.R.; Nino-Baron, C.E.; Strangas, E.G. Overload considerations for design and operation of IPMSMs. *IEEE Trans. Energy Convers.* **2010**, *25*, 921–930. [CrossRef]

13. Ruoho, S.; Kolehmainen, J.; Ikäheimo, J.; Arkkio, A. Interdependence of demagnetization, loading, and temperature rise in a permanent-magnet synchronous motor. *IEEE Trans. Magn.* **2010**, *46*, 949–953. [CrossRef]

14. Tafti, H.D.; Maswood, A.I.; Lim, Z.; Ooi, G.H.P.; Raj, P.H. Proportional-Resonant Controlled NPC Converter for More-Electric-Aircraft Starter-Generator. In Proceedings of the 2015 IEEE 11th International Conference on Power Electronics and Drive Systems, Sindey, Australia, 9–12 June 2015; pp. 41–46.

15. Boglietti, A.; Cavagnino, A.; Tenconi, A.; Vaschetto, S. The Safety Critical Electric Machines and Drives in the More Electric Aircraft: A survey. In Proceedings of the 2009 35th Annual Conference of IEEE Industrial Electronics, Porto, Portugal, 3–5 November 2009; pp. 2587–2594.

16. Moreno-Torres, P.; Lafoz, M.; Blanco, M.; Navarro, G.; Torres, J.; García-Tabarés, L. Switched Reluctance Drives with Degraded Mode for Electric Vehicles. In *Modeling and Simulation for Electric Vehicle Applications*; InTech: London, UK, 2016.

17. Stephens, C.M. Fault Detection and Management System for Fault-Tolerant Switched Reluctance Motor Drives. In Proceedings of the IEEE Transactions on Industry Applications, San Diego, CA, USA, 1–5 October 1989; Volume 27, pp. 1098–1102.

18. Mir, S.; Islam, M.S.; Sebastian, T.; Husain, I. Fault-tolerant switched reluctance motor drive using adaptive fuzzy logic controller. *IEEE Trans. Power Electron.* **2004**, *19*, 289–295. [CrossRef]

19. Hennen, M.D.; Niessen, M.; Heyers, C.; Brauer, H.J.; Doncker, R.W.D. Development and control of an integrated and distributed inverter for a fault tolerant five-phase switched reluctance traction drive. *IEEE Trans. Power Electron.* **2012**, *27*, 547–554. [CrossRef]

20. Moallem, M.; Ong, C.M.; Unnewehr, L.E. Effect of rotor profiles on the torque of a switched-reluctance motor. *IEEE Trans. Ind. Appl.* **1992**, *28*, 364–369. [CrossRef]

21. Bienkowski, K.; Szczypior, J.; Bucki, B.; Biernat, A.; Rogalski, A. Influence of Geometrical Parameters of Switched Reluctance Motor on Electromagnetic Torque. In Proceedings of the XVI International Conference of Electrical Machines-Kraków, Krakow, Poland, 5–8 September 2004; pp. 5–8.

22. Sundaram, M.; Navaneethan, P.; Vasanthakumar, M. Magnetic analysis and comparison of switched reluctance motor with different stator pole shapes using a 3D finite element method. *Simulation* **2009**, *9*, 49–53.

23. Desai, P.C.; Krishnamurthy, M.; Schofield, N.; Emadi, A. Novel switched reluctance machine configuration with higher number of rotor poles than stator poles: Concept to implementation. *IEEE Trans. Ind. Electron.* **2010**, *57*, 649–659. [CrossRef]

24. Bilgin, B.; Emadi, A.; Krishnamurthy, M. Design considerations for switched reluctance machines with a higher number of rotor poles. *IEEE Trans. Ind. Electron.* **2012**, *59*, 3745–3756. [CrossRef]

25. Rallabandi, V.; Fernandes, B.G. Design procedure of segmented rotor switched reluctance motor for direct drive applications. *IET Electr. Power Appl.* **2014**, *8*, 77–88. [CrossRef]

26. Siadatan, A.; Roohisankestani, M.; Farhangian, S. Design and Simulation of a New Switched Reluctance Motor with Changes in the Shape of Stator and Rotor in Order to Reduce Torque Ripple and Comparison with the Conventional Motor. In Proceedings of the 2018 International Symposium on Power Electronics, Electrical Drives, Automation and Motion (SPEEDAM), Amalrfy, Italy, 20–22 June 2018; pp. 353–358.

27. Anvari, B.; Toliyat, H.A.; Fahimi, B. Simultaneous optimization of geometry and firing angles for in-wheel switched reluctance motor drive. *IEEE Trans. Transp. Electrif.* **2017**, *4*, 322–329. [CrossRef]

28. Khalili, H.; Afjei, E.; Najafi, A. Torque Ripple Minimization in SRM Drives Using Phase/Current Profiles. In Proceedings of the 2007 International Aegean Conference on Electrical Machines and Power Electronics, Bodrum, Turkey, 10–12 September 2007; Volume 1, pp. 273–275.

29. Shirahase, M.; Morimoto, S.; Sanada, M. Torque Ripple Reduction of SRM by Optimization of Current Reference. In Proceedings of the 2010 International Power Electronics Conference—ECCE ASIA, Sapporo, Japan, 21–24 June 2010; pp. 2501–2507.

30. Chai, J.Y.; Liaw, C.M. Reduction of speed ripple and vibration for switched reluctance motor drive via intelligent current profiling. *IET Electr. Power Appl.* **2010**, *4*, 380. [CrossRef]

31. Zhang, S.; Li, S.; Harley, R.G.; Habetler, T.G. A Multi-Objective Analytical Design Approach of Switched Reluctance Machines with Integrated Active Current Profile Optimization. In Proceedings of the 2017 IEEE International Electric Machines and Drives Conference (IEMDC), Miami, FL, USA, 21–24 May 2017; pp. 2–7.

32. Ma, C.; Qu, L.; Mitra, R.; Pramod, P.; Islam, R. Vibration and Torque Ripple Reduction of Switched Reluctance Motors through Current Profile Optimization. In Proceedings of the 2017 IEEE International Electric Machines and Drives Conference (IEMDC), Miami, FL, USA, 21–24 May 2017; pp. 3279–3285.

33. Lee, D.; Ahn, S.; Ahn, J. Advanced torque control scheme for the high speed switched reluctance motor. *InTech* **2011**, 87–114. [CrossRef]

34. Krishnan, R. *Switched Reluctance Motor Drives: Modeling, Simulation, Analysis, Design, and Applications*; CRC Press: Boca Raton, FL, USA, 2001.

35. Chithrabhanu, A.; Vasudevan, K. Online Compensation for Torque Ripple Reduction in SRM Drives. In Proceedings of the 2017 IEEE Transportation Electrification Conference (ITEC-India), Pune, India, 13–15 December 2017; pp. 1–6.

36. Li, H.; Bilgin, B.; Emadi, A. An improve torque sharing function for torque ripple reduction in switched reluctance machines. *IEEE Trans. Power Electron.* **2018**, *30*, 8993.

37. Chithrabhanu, A.; Vasudevan, K. An Approach for Vibration Quantification in SRM for Design Studies. In Proceedings of the 2017 National Power Electronics Conference (NPEC), Pune, India, 18–20 December 2017; pp. 25–30.
38. Harikrishnan, R. Improved Online Torque-Sharing-Function based Low Ripple Torque Control of Switched Reluctance Motor Drives. In Proceedings of the 2016 IEEE International Conference on Power Electronics, Drives and Energy Systems (PEDES), Trivandrum, India, 14–17 December 2016.
39. Wei, Y.; Qishuang, M.; Poming, Z.; Yangyang, G. Torque Ripple Reduction in Switched Reluctance Motor Using a Novel Torque Sharing Function. In Proceedings of the 2016 IEEE International Conference on Aircraft Utility Systems (AUS), Beijing, China, 10–12 October 2016; pp. 177–182.
40. Kurian, S.; Nisha, G.K. Torque Ripple Minimization of SRM Using Torque Sharing Function and Hysteresis Current Controller. In Proceedings of the 2015 International Conference on Control Communication & Computing India (ICCC), Trivandrum, India, 19–21 November 2015; pp. 149–154.
41. Chau, K.T. *Electric Vehicle Machines and Drives: Design, Analysis and Application*; John Wiley & Sons: Hoboken, NJ, USA, 2015.
42. Gan, C.; Wu, J.; Shen, M.; Yang, S.; Hu, Y.; Cao, W. Investigation of skewing effects on the vibration reduction of three-phase switched reluctance motors. *IEEE Trans. Magn.* **2015**, *51*. [CrossRef]
43. Ishihara, Y.; Sugiura, M.; Ishikawa, H.; Naitoh, H. Improving the efficiency of switched reluctance motors using a step-skewed rotor. *IEEJ J. Ind. Appl.* **2015**, *4*, 445–453. [CrossRef]
44. Zou, Y.; Cheng, K.-W.E.; Cheung, N.C.; Pan, J. Deformation and noise mitigation for the linear switched reluctance motor with skewed teeth structure. *IEEE Trans. Magn.* **2014**, *50*, 1–4. [CrossRef]
45. Yang, H.Y.; Lim, Y.C.; Kim, H.C. Acoustic noise/vibration reduction of a single-phase SRM using skewed stator and rotor. *IEEE Trans. Ind. Electron.* **2013**, *60*, 4292–4300. [CrossRef]
46. Sugiura, M.; Ishihara, Y.; Ishikawa, H.; Naitoh, H. Improvement of Efficiency by Stepped-Skewing Rotor for Switched Reluctance Motors. In Proceedings of the 2014 International Power Electronics Conference (IPEC-Hiroshima 2014—ECCE ASIA), Hiroshima, Japan, 18–21 May 2014; pp. 1135–1140.
47. Ev Motor-Systems, Co.; Makoto, T.; Takashi, U. Switched Reluctance Motor and Switched Reluctance Motor Drive System. U.S. Patent No 13/529,655, 3 February 1995.
48. Gook, L.H.; Ho, S.J. Multiple-Structured Switched Reluctance Motor. KR20120073341A, 5 July 2012.
49. Shigemitsu, S. Switched Reluctance Motor. JP16005598A, 9 June 1998.
50. Tsukamoto, H.T.M. Reluctance Motor-Integrated Pump. JP3276198A, 16 February 1998.
51. Gizaw, D. Pumping Motor with Skewed Rotor Laminations. U.S. Patent No 09/965,048, 27 Mart 2003.
52. Lewis, M.S. Skewing of Pole Laminations of A Switched Reluctance Machine to Reduce Acoustic Noise. U.S. Patent No 5,266,859, 30 November 1993.
53. Gaing, Z.L. Switching Reluctance Motor and Rotor Thereof. CN104009605A, 12 June 2014.
54. Masamichi, O. Rotor of Rotary Electric Machine. JP2010158453A, 29 November 2012.
55. Moreno-Torres, P.; Lafoz, M.; Navarro, G.; Blanco, M.; García-Tabarés, L.; Torres, J. Procedimiento de Obtención de Una Máquina de Reluctancia Conmutada con Rizado de Par Mejorado. ES2589155A1, 17 August 2017.
56. Miller, T.J.E.; Timothy, J.E. *Switched Reluctance Motors and Their Control*; Hammond, P., Miller, T.J.E., Kenjo, T., Eds.; Oxford Science Publications: Oxford, UK, 1993; Volume 31.
57. Sharifian, M.B.B.; Shaarbafi, K.; Faiz, J.; Feyzi, M.R. Slot Fringing Effect on the Magnetic Characteristics of the Electrical Machines. In Proceedings of the 10th IEEE International Conference on Electronics, Circuits and Systems, Sharjah, United Arab Emirates, 14–17 December 2003; Volume 2, pp. 778–781.
58. Sun, W.; Li, Q.; Liu, K.; Li, L. Design and analysis of a novel rotor-segmented axial-field switched reluctance machine. *CES Trans. Electr. Mach. Sys.* **2017**, *1*, 238–245. [CrossRef]
59. Chen, X.; Wu, J. Calculation of Inductances with 3-D FEM for SRM with Segmental Rotors and Fully-Pitched Windings. In Proceedings of the 2014 17th International Conference on Electrical Machines and Systems (ICEMS), Hangzhou, China, 22–25 October 2014; pp. 1822–1824.
60. Deshpande, U. Two-dimensional finite-element analysis of a high-force-density linear switched reluctance machine including three-dimensional effects. *IEEE Trans. Ind. Appl.* **2000**, *36*, 1047–1052. [CrossRef]
61. Ansys Ansys Maxwell: Low Frequency Electromagnetic Fields. Available online: http://www.ansys.com/products/electronics/ANSYS-Maxwell (accessed on 23 October 2017).
62. Zhang, J.; Radun, A.V. A new method to measure the switched reluctance motor's flux. *IEEE Trans. Ind. Appl.* **2006**, *42*, 1171–1176. [CrossRef]
63. Mehta, S.; Kabir, A.; Husain, I. Decoupled Modeling of Mutually Coupled SRM Based on Net Flux Method. In Proceedings of the 2018 IEEE Transportation Electrification Conference and Expo (ITEC), Long Beach, CA, USA, 13–15 June 2018; pp. 114–118.
64. The Mathworks Inc. MATLAB—MathWorks. Available online: http://www.mathworks.com/products/matlab/ (accessed on 21 October 2017).
65. Pyrhönen, J.; Jokinen, T.; Hrabovcová, V. *Design of Rotating Electrical Machines*; John Wiley & Sons: Hoboken, NJ, USA, 2013.
66. Torres, J.; Moreno-Torres, P.; Navarro, G.; Blanco, M.; Lafoz, M. Fast energy storage systems comparison in terms of energy efficiency for a specific application. *IEEE Access* **2018**, *6*, 40656–40672. [CrossRef]
67. *SEMiX305GD07E4 SEMiX305GD07E4*; SEMIKRON: Nuremberg, Germany, 2017.

68. Das, S.; Suganthan, P.N. Differential evolution: A survey of the state-of-the-art. *IEEE Trans. Evol. Comput.* **2011**, *15*, 4–31. [CrossRef]
69. Blanco, M.; Lafoz, M.; Ramirez, D.; Navarro, G.; Torres, J.; Garcia-Tabares, L. Dimensioning of point absorbers for wave energy conversion by means of differential evolutionary algorithms. *IEEE Trans. Sustain. Energy* **2018**, *10*, 1076–1085. [CrossRef]
70. Oksuztepe, E. In-wheel switched reluctance motor design for electric vehicles by using a pareto-based multiobjective differential evolution algorithm. *IEEE Trans. Veh. Technol.* **2017**, *66*, 4706–4715. [CrossRef]
71. Srinivas, N.; Deb, K. Muiltiobjective optimization using nondominated sorting in genetic algorithms. *Evol. Comput.* **1994**, *2*, 221–248. [CrossRef]